Proceedings of ASME Turbo Expo 2011
GT2011
June 6-10, 2011, Vancouver, British Columbia, Canada

GT2011-46796

AUTOMOTIVE TURBOCHARGER COMPRESSOR CFD AND EXTENSION TOWARDS INCORPORATING INSTALLATION EFFECTS

Onur Baris
Ford OTOSAN,
Gebze Engineering
Gebze, Kocaeli, Turkey

Fred Mendonça
CD-adapco
200 Shepherds Bush Road
London
UK

ABSTRACT

This paper focuses on the application of CFD to turbocharger compressor characteristics predictions over a range of speeds between 100,000 and 200,000RPM, and concentrating around the peak performance at 160,000RPM. A production turbocharger compressor which is widely used in the small-to-medium size automotive sector is studied. A methodical approach is taken to compare computation versus rig measurements, which represents an idealised installation.

Benchmarking under the idealised rig conditions then gives a degree of confidence to apply the same prediction method to the device under real installation conditions. In practice this means that the inlet duct is strongly curved due to space constraints. One observes that the performance of the compressor deteriorates at higher mass flows when the inflow to the compressor face is distorted by a curvilinear duct. Under the same installation constraint, we then observe that performance reduces when using inlet guide vanes upstream of the compressor face to alleviate noise problems.

A primary motivator in this work is to develop an efficient methodology for analysing the turbocharger compressor performance. To do this it is necessary first to benchmark the CFD methodology in steady-state so that the OEM can be confident to perform intake design analyses for their vehicles under installation conditions. Therefore we concentrate here on robust processes for geometry handling, meshing and flow solution which can be easily automated.

NOMENCLATURE

ω - specific dissipation rate (s^{-1}) a transported quantity in RANS two-equation turbulence modelling
ε - turbulence dissipation rate ($m^2.s^{-3}$) a transported quantity in RANS two-equation turbulence modelling
ρ - density ($kg.m^{-3}$)
u_τ - friction velocity ($m.s^{-1}$), $= \sqrt{(\tau_w/\rho)}$
τ_w - wall shear stress (Pa.s)
Re - Reynolds Number (dimensionless), measure of the ratio of inertial to viscous forces. "Low-Re" refers to fine wall boundary-layer resolution down to the laminar sub-layer. "High-Re" refers to coarse wall-resolution only to the log-law part of the boundary-layer utilising wall-functions.
k - turbulence kinetic energy ($m^2.s^{-2}$), a transported quantity in RANS turbulence modelling
IGV - Inlet Guide Vanes
MRF - Multiple Rotating Frames
OEM - Original Equipment Manufacturer
RPM - revolutions per minute
SST - Shear Stress Transport
y^+ - Dimensionless measure of the near-wall distance $= yu_\tau/\upsilon$

1. INTRODUCTION

A challenge to automotive OEMs is to take supplier equipment, tested in idealized conditions, and install them in geometrically complicated engine assemblies. Space management often leads to flow conditions which deviate significantly from test conditions. In the case of turbocharger compressors, this can lead to distortions at the inflow to the compressor face and consequently compromise the device's performance.

As it is impractical to make device performance measurements for a wide permutation of possible engine installations and different vehicle derivatives, CFD offers a unique potentially in the form of virtual testing. Radial compressor performance prediction has been the subject of numerous successful CFD studies. For example, Grigoriev et al, 2010 [1] reports on the benchmarking of the same CFD software [2] used in this study, using a hierarchy of simulations methodologies, starting from steady-state on a single-blade in the wheel, to transient sliding mesh on the complete stage, including full wheel, diffuser vanes and scroll.

Two challenges remain. First, incorporating detailed geometries with respect to the turbocharger wheel; leakage paths, tip clearance, fillets and chamfers, not least to say obtaining a CAD representation of the geometry. Secondly, CFD solutions are more difficult to obtain as the device operation approaches the surge line. On the face of it, this is understandable because steady-state CFD naturally suffers from 'convergence' issues at the low mass-flows where the flow regime becomes unsteady. Transient calculations should by their nature be more applicable - however this comes at a significant computational penalty.

In this paper, we demonstrate for a small-to-mid-size automotive turbocharger compressor that steady-state computations can be successful fairly close, but not all the way to the surge line. Extension to transient flow using canonical RANS-based turbulence models, e.g. [3], and more complex alternatives (towards Large Eddy Simulation) is beyond the scope of this initial assessment, but will form the focus of future studies.

The following sections describe the use of commercial CFD used at Ford to predict the complete performance curve of a production turbocharger compressor, under a wide range of operating conditions. There are advantages to using commercial tools for such applications, mainly due to their recognized ability to deal with complex geometries, ease of use, robustness and repeatability [4-7]. Repeatability in a design and production environment allows for virtual modeling to take its place as a valuable support to experimental programmes, and in extreme circumstances, to provide performance data which is experimentally impractical or prohibitively expensive. A nominal disadvantage of using commercial codes is their generality, which needs benchmarking against specific turbo-machines.

Section 2 describes in detail the compressor studied under idealised and installation conditions. Section 3 covers the CFD methodologies, including geometry handling, meshing and flow model settings. In Section 4, we enumerate the device performance operations against which the CFD is first benchmarked under ideal installation conditions and compare the CFD against rig measurements.

Then in Section 5, we extend the predictive modeling only towards illustrating along the peak efficiency speed-line a degradation of the performance of the compressor under real-installation conditions. Curved inlet ducts result in a distortion at the compressor face, creating a noise problem. Furthermore, we demonstrate a subsequent change in the performance with the use of compressor inlet guide vanes. Previous studies report on adding positive and negative swirl upstream of the compressor face [8]. Pre-swirl vanes are added here to alleviate the noise problems.

2. TURBOCHARGER COMPRESSOR; IDEALISED AND IN-SITU CONFIGURATIONS

Figure 1 shows the compressor volute and wheel of diameter 45mm comprising 6 main and 6 splitter blades.

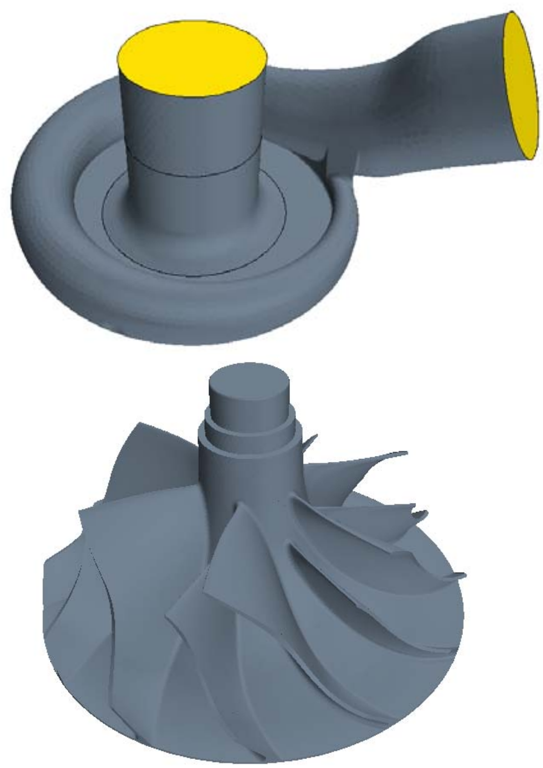

Figure 1: Volute and diffuser (top), wheel (bottom)

In the test rig the compressor assembly is fitted with straight inlet and outlet sections of constant diameter upstream and downstream of the wheel and volute/diffuser. The CFD computations for the idealized configuration are performed on the geometry shown in Figure 2. Figure 3 shows a real installation, in which the inlet duct is strongly curved, and Figure 4, the same ducting with pre-swirl inlet guide vanes.

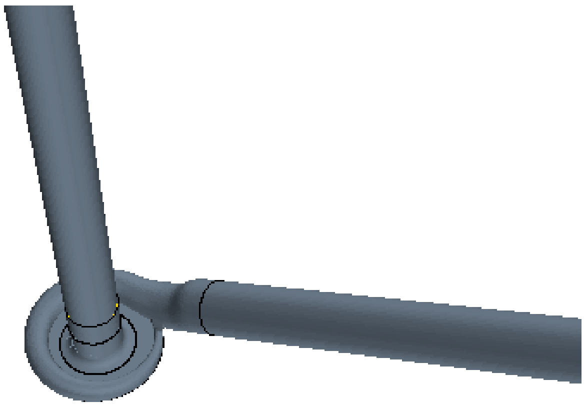

Figure 2: Ideal installation

Figure 3: In-situ configuration

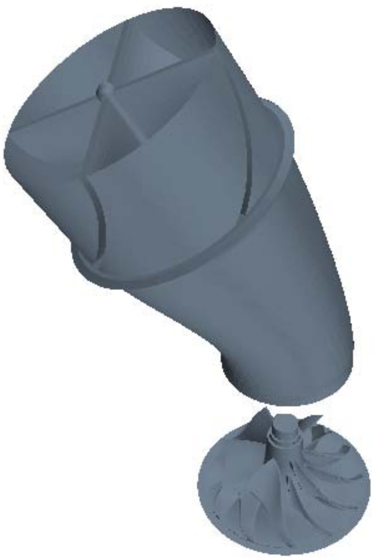

Figure 4: In-situ configuration with pre-swirler

This turbocharger operates typically between 100,000 and 200,000RPM, achieving peak performance in the middle of that range. Benchmarking of the predictions was performed at these extreme rotation rates. Then based on the rig performance curves, we selected 160,000RPM as an intermediate speed for the ideal installation and two variants; curved inlet without and with the inlet guide vanes.

3. CFD METHODOLOGIES

CAD, Geometry and Surface Meshing

All component geometries, wheel, housing, volute, diffuser, inlet and exit sections, were defined via CAD as IGES parts. Though the IGES representation is automatically tessellated, it inevitably contains a large number of surface imperfections such as elongated triangulations, edge overlaps and voids that are not a suitable basis for volume meshing.

These can be cured in the software using inbuilt tools based on surface-wrapping technology and surface re-triangulation. Figure 5 illustrates the re-triangulated surface on the main and splitter blades, concentrating the triangles near the leading and trailing edges of the blades, tip and fillet, faithfully representing the original CAD imported tessellation shown in Figure 1.

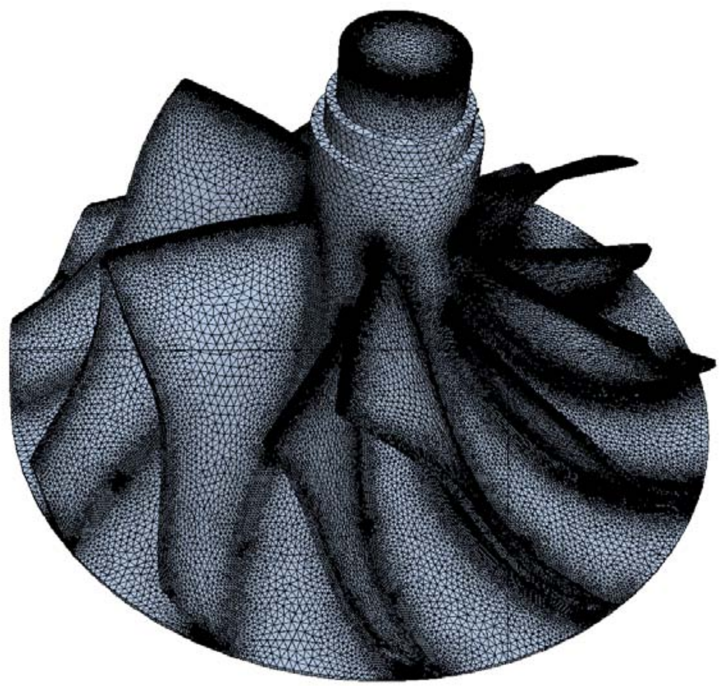

Figure 5: Surface re-triangulation

The surface repair tools have sufficient control to allow the analyst to choose which components to include and exclude (de-feature) in the meshing, to control the size of the triangulations in various parts by using surface curvature or by defining local refinement zones. Once these surface mesh control settings have been set by the analyst, the tool retains the association with the imported CAD part. This makes parametric modelling of components very easy. If a part or component is modified, a new CAD importation of that part simply replaces the existing model geometry definition while retaining its previously associated meshing settings.

Volume meshing

The volume mesh is generated using arbitrary polyhedra, as validated for flow and thermal solutions [4-7]. A polyhedral cell comprises typically 12-16 faces, agglomerated from an underlying automatically generated tetrahedral mesh. Polyhedral meshes offer significant advantages over traditional mesh types. As with tetrahedral meshes and unlike hexahedra, they can be automatically generated. Polyhedral meshes exhibit far less numerical diffusion compared with tetrahedral because of the greater likelihood of face alignment to the flow. Gradient calculations are more accurate due to the greater number of face neighbours. Cell counts are typically a third of the equivalent tetrahedral meshes for similar fineness of resolution. All these mean that polyhedral meshes run faster, are more accurate and converge more robustly than tetrahedral meshes [4].

Figure 6 shows a slice through the rotational plane, and illustrates a schematic of the normal-to-wall extrusion layers in the boundary layer of the blade and casing. The bottom image shows that this meshing methodology automatically accommodates the blade-shroud clearance, pinching the thickness of the near-wall extrusion in the very small clearance gap.

The re-meshed triangulated surface is first inflated to a user-controlled distance equivalent to the boundary layer or required extrusion-layer thickness. Surface inflation contains sufficient intelligence to account for close-proximity surface and inside edges, where the extrusion-layer is automatically squeezed as the surfaces approach (see Fig.6. bottom). The remaining volume is meshed with tetrahedra. Automatic refinement is carried out in areas of curvature and close geometric proximity to ensure that a user-controlled number of cells will span any gap. The inflated surface triangulation is then extruded back to the original surface using user specified controls for near-wall cell height and normal-to-wall expansion factor. Polyhedra are then generated from dualization of the tetrahedral and triangular-prism based mesh.

The near-wall cell height is chosen to be compatible with the usual range typical for application of the y+ independent wall-function, with y^+ less than 20 for all three speeds studied. Figure 7 shows the distribution of y+ on the wheel. Three wall-layers are applied with a total thickness of 0.5mm and a wall-normal growth rate of 1.2.

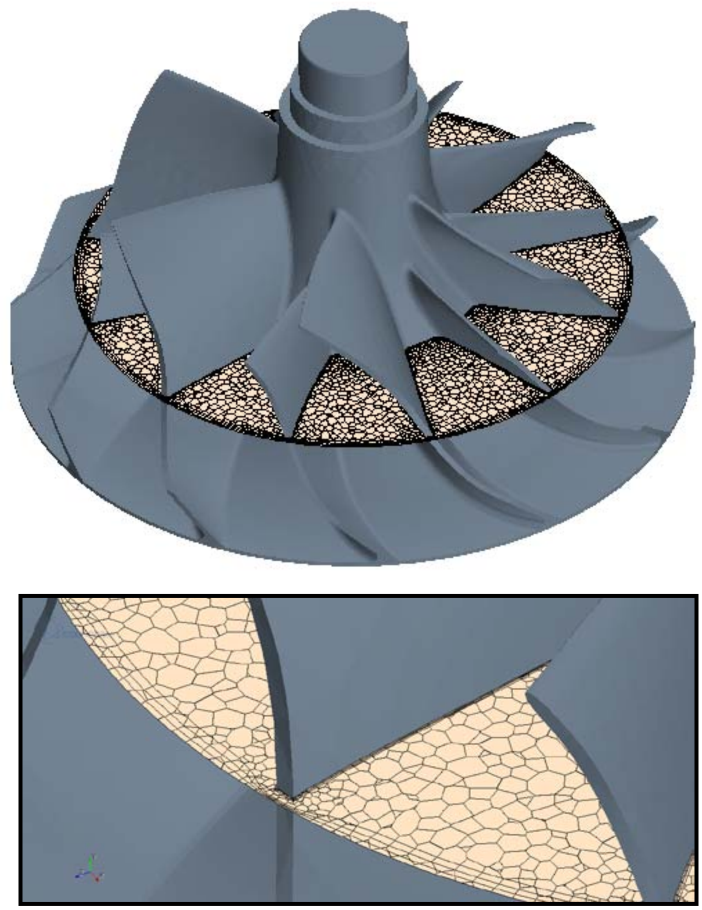

Figure 6: Volume polyhedral mesh (top), section (middle) and wall detail (bottom)

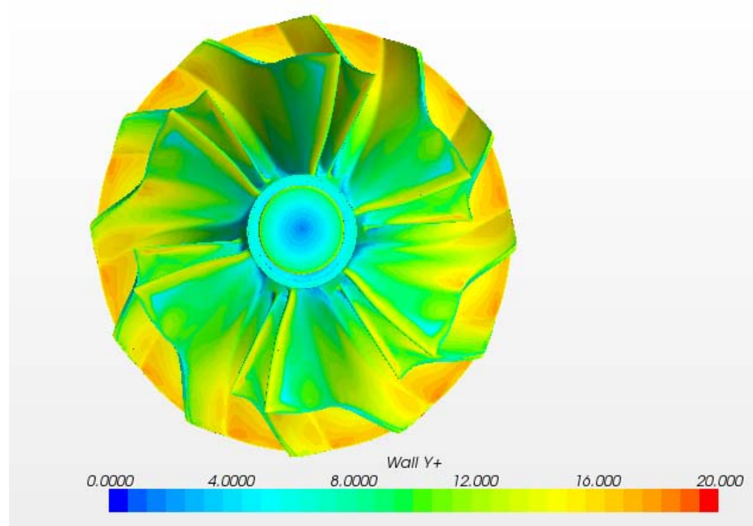

Figure 7: typical y+ at 160,000RPM

Flow Modelling

STAR-CCM+ [2] uses a compressible implicit coupled algorithm. The domain is split into two parts, one enveloping all the rotating parts (blades and hub) and the other the static parts (shroud, guide vanes, inlet and outlet ducting). Consequently, the system is solved using multiple rotating frames of reference (MRF).

A mixing-plane interface treatment is used at the interface between the static and rotating parts. The mixing plane interface applies a commonly used treatment which circumferentially averages out the velocities along several radial bands at the outlet of the upstream domain and applies the mean circumferential velocity value to each radial band at the inlet of the downstream domain. Conversely, the average circumferential pressure on several radial bands at the inlet to the downstream domain is applied to the exit of the upstream domain. This treatment allows for mean radial variations.

Turbulence is modelled using the k-ω-SST model [3]. This model is a zonal combination of k-ω near the wall, nominally in the boundary layer, and k-ε away from walls. When the near-wall mesh is compatible with the wall-function approach, this model behaves predominantly as a high-Reynolds number k-ε formulation.

All surfaces are treated as adiabatic. Total pressure and total temperature are applied at the upstream inlet boundary, and to atmospheric conditions. The downstream condition is set to static pressure.

For a given compressor speed, the first operating point in the sequence is chosen at the lowest pressure ratio close to the choke condition. Subsequent operating points are re-started from this condition with an increased downstream pressure, then successively ramped up to achieve the higher pressure ratios towards the surge line. One observes that steady-state convergence characteristics deteriorate as the turbocharger operation approaches stall, due the onset of flow unsteadiness. Unsteady calculations are outside the scope of this investigation, but will be the focus of future work beyond this present benchmarking.

The models contain roughly 2,000,000 cells, each operating point at each speed takes approximately 3 hours to run on a 32-core Linux machine.

4. BENCHMARKING: IDEALISED CONFIGURATION

Three speeds are considered, two corresponding to the extremes of operation at 100,000RPM and 200,000RPM. The third, 160,000RPM was selected to be close to the peak efficiency of operation.

Results

Figure 8 shows the predicted compressor characteristic at the three speeds investigated versus the rig measurements. The calculations at low pressure ratio points for all speeds correspond very closely in predicted mass-flow to the measurements.

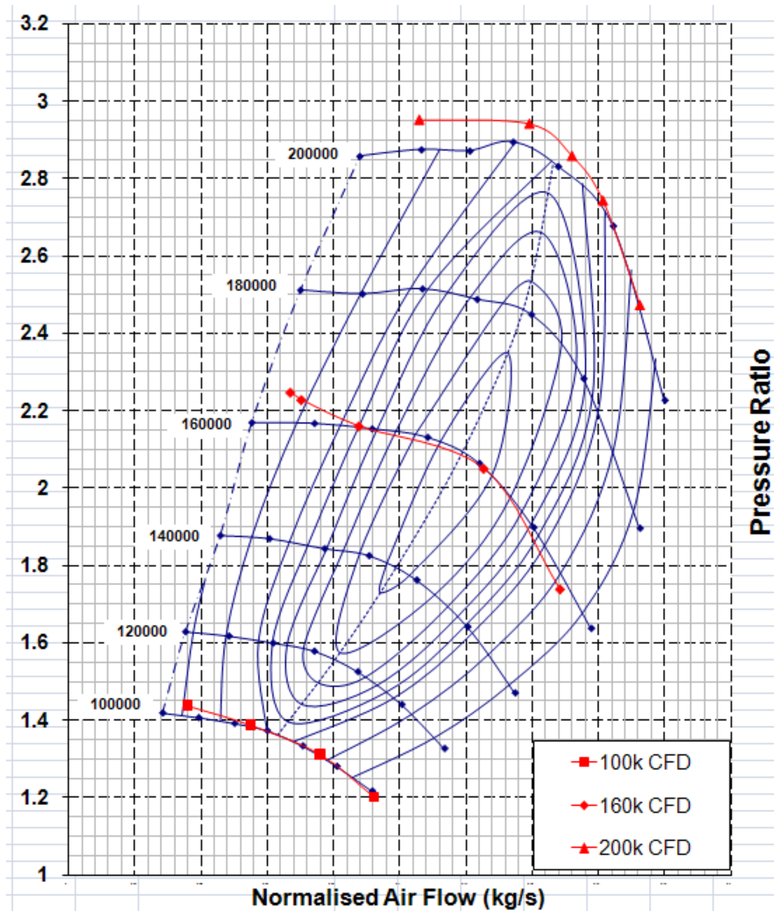

Figure 8: Compressor pressure ratio vs. mass-flow

At the highest efficiencies for each speed line, the 100,000 and 160,000RPM predictions are in good agreement with the experiments, within 1%, whereas at the highest speed, 200,000RPM deviation from the measurements of 2-3% is observed. At the higher pressure ratios, and especially near the surge line, the deviation is up to 3.5% over-prediction at any given speeds.

Over-prediction of the pressure rise is a common feature of these predictions at the low mass flows for all speeds. If we consider that flow separation in the blade passage is a characteristic of the low mass-flow regime approaching surge, this suggests either that the wall-function RANS-based CFD is failing to capture flow separation quickly enough with respect to increasing pressure ratio, or that "unsteadiness" in the predicted steady-state CFD somehow changes the nature of the predicted mean flow enough to cause the observed over-prediction.

To substantiate this point, Figure 9 shows the residuals for two operating points along the 160,000RPM speed line, approaching surge. The first, at a pressure ratio of 2.15, converges to a residual level which has reduced five or six decades. The corresponding mass-flow flat-lines. However, the second, at PR above 2.2, cannot be considered to be fully steady in the sense of many decades of residual reduction and unchanging mass-flow, yet the mean levels or residuals flatten off, as does the associated mass-flow to the value reported, with a small oscillation around the mean due to the predicted "unsteadiness". Consequently, for all the operating points presented here, the reported mean measure of mass flow is considered to be converged.

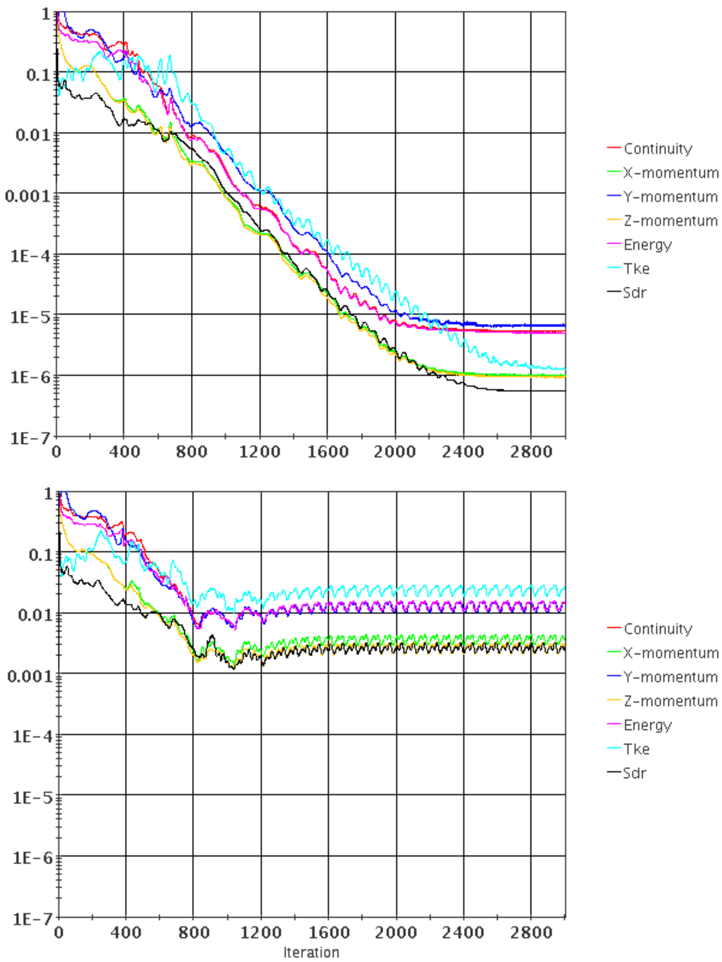

Figure 9: Global normalised residual behaviour approaching stall, 160,000RPM at PR=2.15 (top) and 2.25 (bottom)

The only way to resolve these issues associated with steady-state CFD is to run fully time-accurate unsteady CFD. This is beyond the scope of the present study, in which the main objective is to benchmark the code behaviour using automated, batch-driven, fast CFD methodology in steady-state. Characterising the CFD behaviour in the transient regime close to stall will form the basis of further work.

Figure 10 provides insight into the onset of unsteadiness as the characteristic approaches stall for the 160,000RPM speed line. The succession of images from high to low mass-flow show the "surface streamlines" on the main and splitter blade suction surfaces.

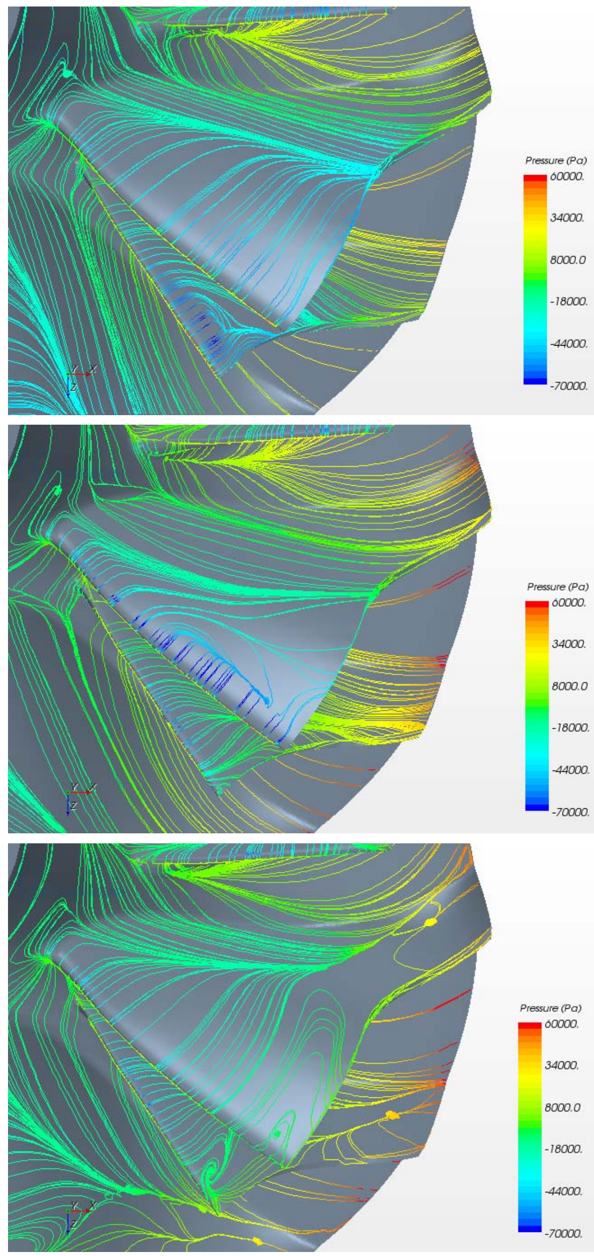

Figure 10: Surface Streamlines coloured by static pressure, 160,000RPM with increasing pressure ratio 1.73(top), 2.15 (middle) and 2.25 (bottom)

The flow is fully attached on main blade suction surface at the highest mass-flow, with some small signs of separation on the splitter blade near the leading edge towards the shroud. At the higher pressure ratio (2.15), which is beyond peak efficiency, a strong shroud-wise three-dimensional separated flow is observed on the splitter blade suction surface, whereas separation has commenced on the midspan-to-shroud extent of the main blade near the leading edge. At the highest pressure ratio (2.25), the flow has become strongly separated and highly three-dimensional on both main and splitter blades in the shroud region. Large parts of the flow still remain attached, which could explain the increasing pressure rise at flow rates close to surge.

Figure 11 compares the axial velocity distributions just upstream of the compressor face for the five points on the 160,000RPM speed line plotted on the compressor characteristic (Figure 8). It confirms that the shroud flow has separated at the highest pressure ratio.

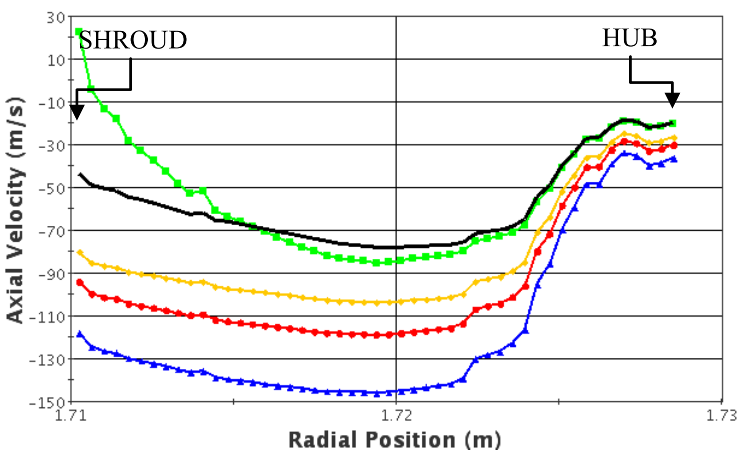

Figure 11: Axial Velocity profiles, ideal installation, 160,000RPM;
PR ▲ = 1.73; ● = 2.05; ◇ = 2.15; ▬ = 2.23; ■ = 2.25

For the purpose of benchmarking, Figure 8 provides sufficient justification of the CFD methodologies enumerated, with the noted caveats close to surge to be further investigated in future studies.

5. EXTENSION TO IN-SITU CONFIGURATION

In this section, the same methodologies are applied to the in-situ geometrical configurations shown in Section 2 at the operating speed of 160,000RPM which crosses the peak performance island.

Figures 12 compares the predicted ideal configuration characteristic with the in-situ predictions without and with IGV. We see a slight deterioration in the performance of the compressor when the upstream straight pipe is fitted with a strongly curved inlet duct representative of a real installation (in-situ no-IGV). At peak performance, the prediction reports a 2% drop in PR rise. Fitting the pre-swirl vanes leads to a further deterioration in the pressure rise to 5% less than the ideal installation.

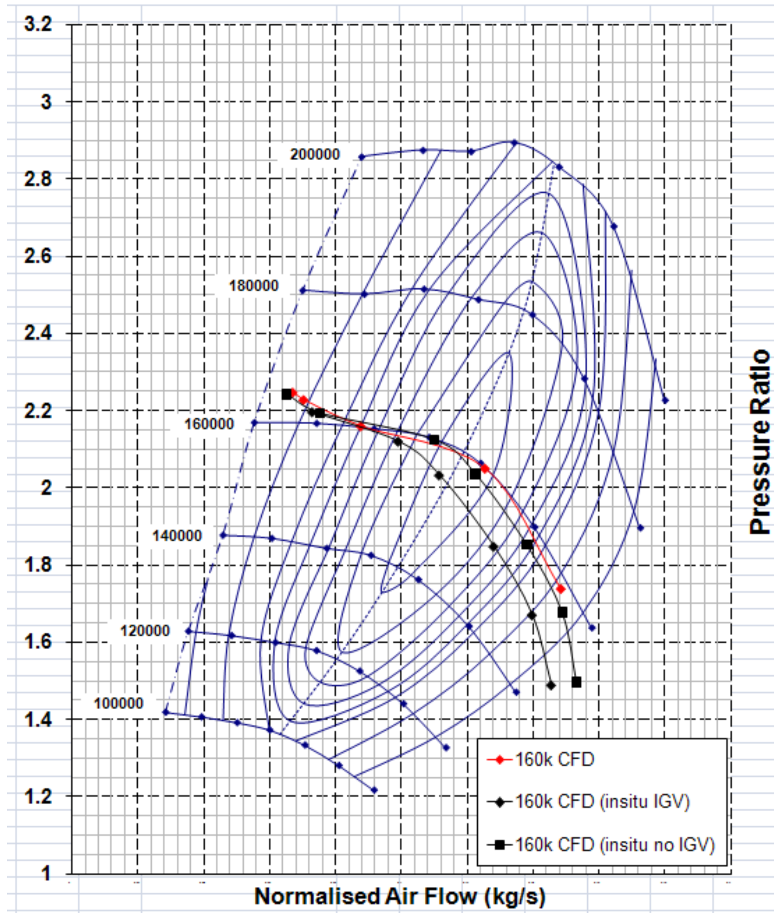

Figure 12: Compressor pressure ratio vs. mass-flow - Ideal versus In-situ configurations

The following figures attempt to explain the behaviour by analysing the three operating points near peak performance at PR~2.05 for the three cases considered.

Figure 13 shows contours of the axial velocity and velocity vectors at a plane just upstream of the compressor face (shown in yellow, Figure 1 (top)) in the static upstream part of the computational domain. The distortion in axial velocity profile caused by the curved inlet duct is apparent. Acoustically, this distortion is "first order", meaning that a disturbance is experienced once every rotation. At rotation speeds between 100,000RPM and 200,000RPM, this disturbance will be manifested at between 1,667Hz and 3,333Hz which corresponds almost exactly with the peak human audibility range. This will clearly be a cause of annoyance to the customer, and is therefore a problem which the OEM is obliged to address [9]. The pre-swirl vane is added upstream of the compressor face to reduce the velocity distortion, and consequently also to reduce the acoustical first order mode, by mixing the flow upstream of the compressor face through the introduction of swirl. In this case, swirl is induced in the same rotation direction as the wheel rotation. Figure 13 (bottom) shows clearly the induced swirl compared with the no-IGV case. Also apparent is the improvement to the axial velocity distortion generated by the pre-swirl guide vales. Future transient studies will seek to quantify these acoustical effects.

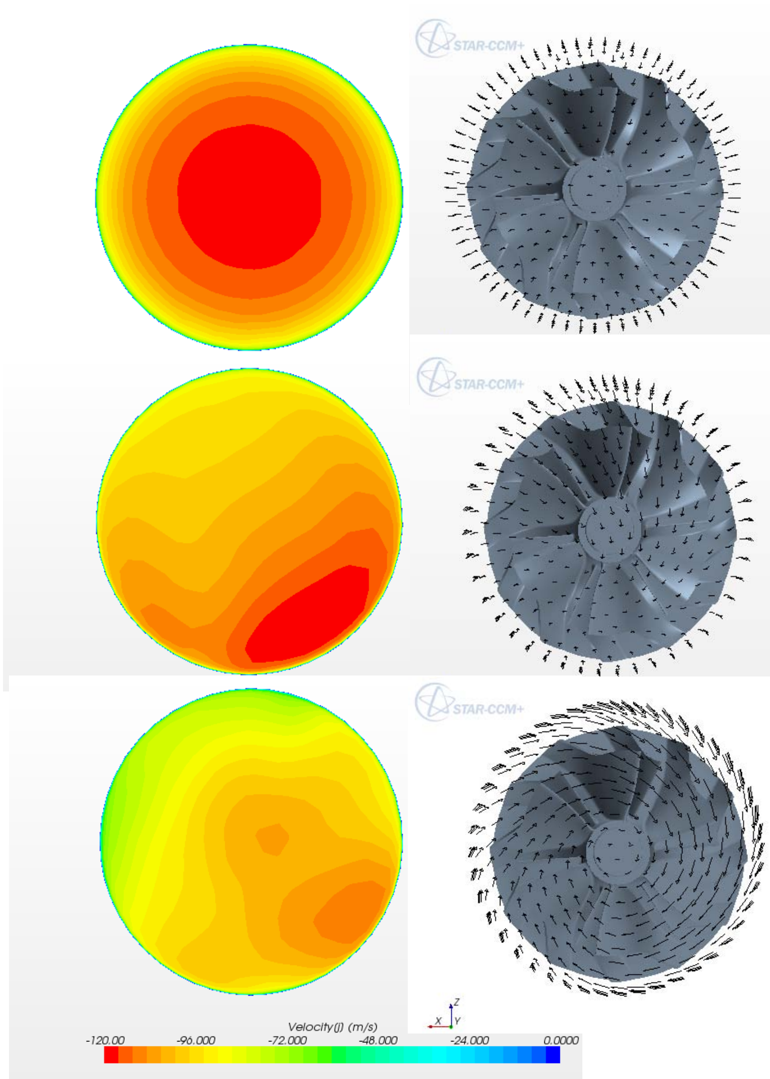

Figure 13: Axial velocity profiles and vectors, ideal installation (top), in-situ without IGV (middle), and in-situ with IGV (bottom) at 160,000RPM and Pr~2.05

Figure 14 (as Figure 11) compares the axial velocity distributions just upstream of the compressor face for the three geometries assessed at PR close to 2.05. These profiles are taken downstream of the mixing-plane interface after the circumferential averaging has been performed along several radial bands.

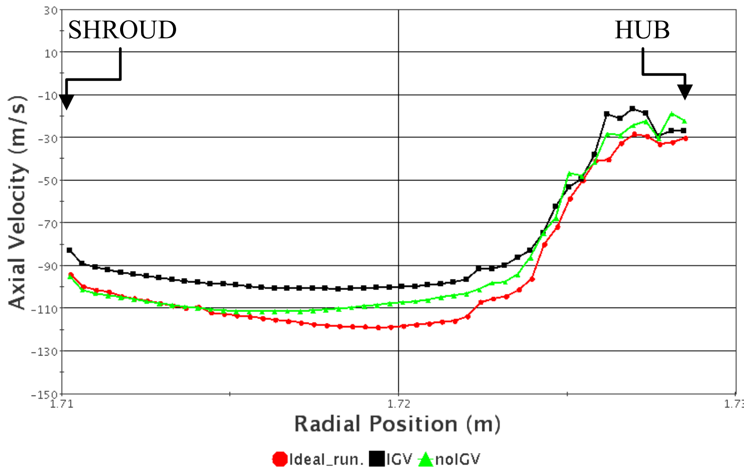

Figure 14: Axial Velocity profiles, ideal installation versus curved inlet without and with IGV, PR~2.05 at 160,000RPM

The curved duct distortion causes a radial redistribution of the axial velocity profile seen by the compressor face, in particular a reduced axial velocity at the inner radius. From Figure 15, it is almost impossible to see any change in flow inclination approaching the main compressor blade leading edge due to the curved duct or pre-swirl vane.

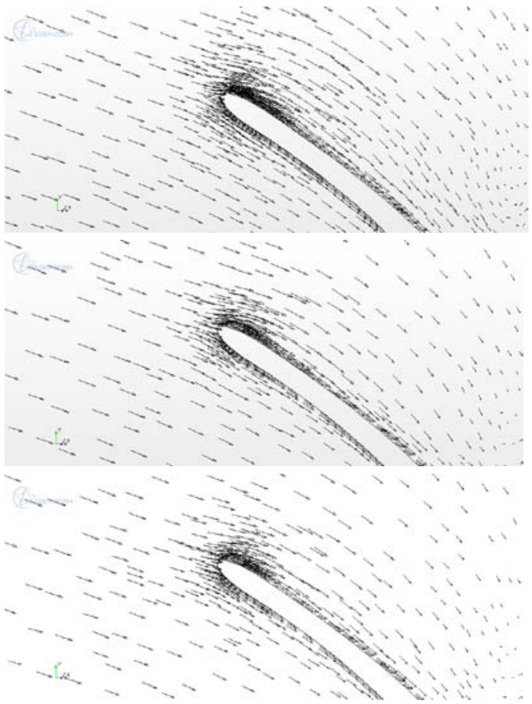

Figure 15: Flow inclination at ~90% span of the main compressor blade; ideal installation (top), in-situ without IGV (middle) and in-situ with IGV (bottom)

The effect is seen in Figure 16 (middle) where a flow separation occurs along the main blade leading edge causing a loss in pressure rise at peak performance. The leading edge separation is eliminated by the use of the pre-swirl vane which reduces the angle of attack at the leading edge of the compressor blades. However, the presence of the IGV creates an additional pressure drop which reduces the device performance still further.

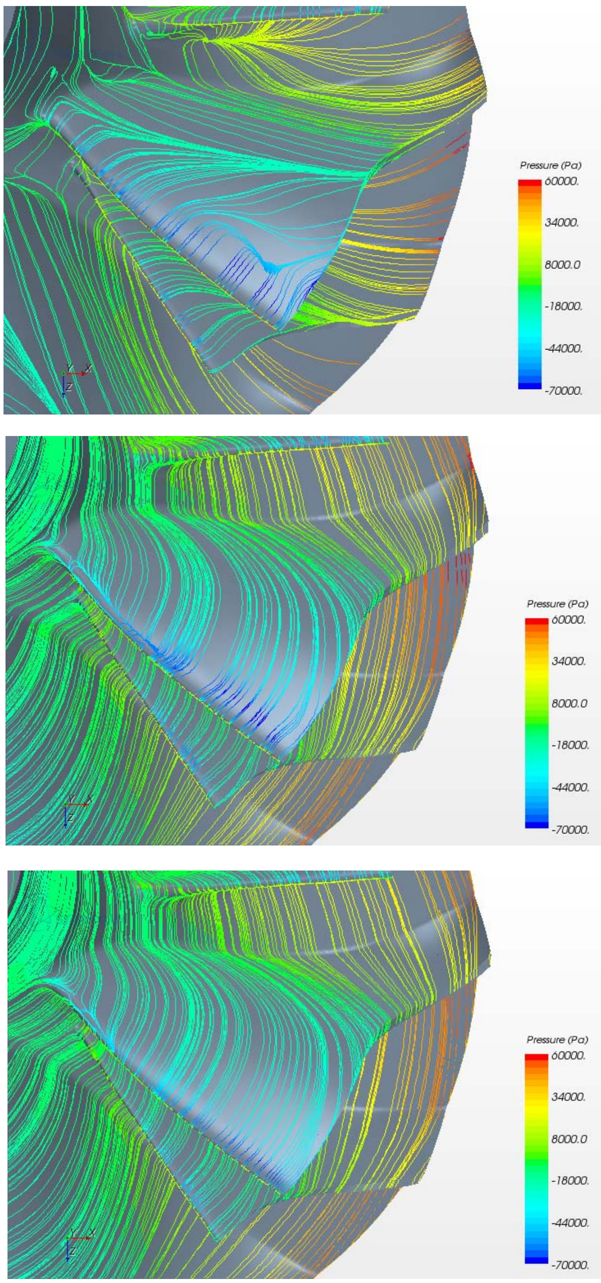

Figure 16: Surface Streamlines coloured by static pressure, 160,000RPM at PR~2.05 (peak efficiency);ideal installation (top), in-situ without IGV (middle) and in-situ with IGV (bottom)

6. CONCLUSIONS

The present work benchmarks the use of CFD for predicting the performance of mid-size automotive turbocharger compressors at Ford. Adequate levels of accuracy, within 2% of measurements in an idealised installation rig, are achieved for a wide range of operating speeds and across the speed line between choke and beyond peak performance. Discrepancies of up to 3.5% occur close to the surge line where it is likely that the steady-state CFD methodologies adopted are less applicable. The benchmarking under ideal rig conditions is an important step in justifying the modelling techniques employed - compressible flow using a canonical two equation turbulence model with high-Re wall-function based modelling. This method has been shown to be robust, repeatable and is automated, and is therefore a valuable tool for the designer of automotive air intake systems.

The same methodology has then been extended to non-ideal installations, characterised by a strongly curved inlet duct which causes a strong distortion to the inflow at the compressor face. This deteriorates the performance of the device and creates a potentially annoying acoustical disturbance at a frequency corresponding to the rotation speed. Introducing pre-swirl vanes reduces the inflow distortion at the expense of a further performance deterioration.

Future work will concentrate on extending the predictive capabilities closer to the stall line, by performing transient calculation where it is clear that the flow is no longer steady. Transient calculations will additionally offer an insight in to the aeroacoustical effects or distortion on the compressor face.

ACKNOWLEDGEMENTS

The authors express thanks to A. Peck and R. Fitzsimmons, CD-adapco, for their assistance in the development of the automated process used in this work.

REFERENCES

[1] Grigoriev M, Swiatek C and Hitt J, **"Benchmarking CD-adapco's STAR-CCM+ in a Production Design Environment"**, GT2010-23627, Proceedings of ASME Turbo Expo 2010, Glasgow, UK.

[2] **STAR-CCM+,** release version 5.04, CD-adapco, June 2010, www.cd-adapco.com,

[3] F. Menter, **"Two-Equation Eddy Viscosity Models for Engineering Applications"**, AIAA Journal, Vol. 32, No. 8, 1994, pp. 1598-1605

[4] M. Peric, **“Flow simulation using control volumes of arbitrary Polyhedral shape”**, *ERCOFTAC Bulletin 62*, September 2004

[5] I. Demirdžić, S. Muzaferija, **“Numerical method for coupled fluid flow, heat transfer and stress analysis using unstructured moving meshes with cells of arbitrary topology”**, *Comput. Methods Appl. Mech. Engrg.*, **125**: 235-255, 1995.

[6] J. Davison, S. Ferguson, F. Mendonça, A. Peck **"Towards an automated simulation process in combined Thermal, Flow and Stress in Turbine Blade Cooling Analysis",** GT2008-51287, ASME Turbo Expo, Berlin, 2008

[7] Mendonça F, Clement J, Palfreyman D and Peck A, **"Validation of Unstructured CFD Modelling Applied to the Conjugate Heat Transfer in Turbine Blade Cooling"**, ETC_8-198, European Turbomachinery Conference, Graz, 2008

[8] Xiao J, Gu C, Shu X and Gao C, **"Performance analysis of a centrifugal compressor with variable inlet guide vanes"**, Front. Energy Power Eng., China 2007, 1(4): 473-476

[9] Mendonça F., Chapter on **"Industrial Aeroacoustics Analyses"** in *LES for Acoustics*, Cambridge University Press, 2007, ISBN: 978-0-521871-44-0

